

This item is the archived peer-reviewed author-version of:

Evaluation of an anthropometric shape model of the human scalp

Reference:

Lacko Daniël, Huysmans Toon, Parizel Paul M., De Bruyne Guido, Verwulgen Stijn, Van Hulle Marc M., Sijbers Jan.- *Evaluation of an anthropometric shape model of the human scalp*

Applied ergonomics - ISSN 0003-6870 - 48(2015), p. 70-85

DOI: <http://dx.doi.org/doi:10.1016/j.apergo.2014.11.008>

Evaluation of an anthropometric shape model of the human scalp

Daniël Lacko^{a,b,c,*}, Toon Huysmans^a, Paul M. Parizel^d, Guido De Bruyne^b, Stijn Verwulgen^b, Marc M. Van Hulle^c, Jan Sijbers^a

^a*Minds-Vision Lab, University of Antwerp, Antwerp, Belgium*

^b*Department of Design Science, Product Development, University of Antwerp, Antwerp, Belgium*

^c*Laboratorium voor Neuro- en Psychofysiologie, KU Leuven, Leuven, Belgium*

^d*Department of Radiology, Antwerp University Hospital & University of Antwerp, Antwerp, Belgium*

Abstract

This paper presents the evaluation a 3D shape model of the human head. A statistical shape model of the head is created from a set of 100 MRI scans. The ability of the shape model to predict new head shapes is evaluated by considering the prediction error distributions. The effect of using intuitive anthropometric measurements as parameters is examined and the sensitivity to measurement errors is determined. Using all anthropometric measurements, the average prediction error is 1.60 ± 0.36 mm, which shows the feasibility of the new parameters. The most sensitive measurement is the ear height, the least sensitive is the arc length. Finally, two applications of the anthropometric shape model are considered: the study of the male and female population and the design of a brain-computer interface headset. The results show that an anthropometric shape model can be a valuable tool for both research and design.

Keywords: computer-aided design, shape modeling, product development, anthropometry, population study

1. Introduction

Parametric shape modeling is a popular technique to describe a population of 3D shapes with a limited set of parameters [1]. When applied to the human body, it enables

*Corresponding author: Phone: +3232652472 Fax: +3232652245
Email address: daniel.lacko@uantwerpen.be (Daniël Lacko)

medical doctors, product designers and researchers to study the human body through
5 high-quality 3D representations [2]. For the sake of simplicity, people working in these
fields will be referred to as 'ergonomists' throughout the remainder of this article. The
parameters that yield the most accurate shape predictions of the body are usually found
by statistically analyzing a sample of 3D polygonal surfaces. Although the resulting
statistical shape models (SSM) accurately describe the object's shape, these statistics
10 are often difficult to interpret and non-intuitive for design specialists. Therefore, several
methods have been proposed to compute a new set of parameters to characterize the
human body shape. Most of them were focused on the full body [3, 1, 4, 5, 6], the
face [7] or head [8]. This research shows that head shapes can indeed be predicted from
either semantic parameters such as age, gender and ethnicity or from various body size
15 measurements.

While more recent techniques were suggested as solutions for industrial designers
[9, 10, 8, 5], it is not clear how they should interpret and use the results. Custom
GUI applications have been suggested, in which the model can be varied according to
statistical parameters [11, 12]. However, statistical parameters are not intuitive enough
20 to be used by ergonomists. Other suggestions include generating 3D models based on
anthropometric measurements and then using these static shapes in 3D software [13],
which is not far off from traditional anthropometry. Furthermore, only the average
geometric (i.e. vertex-to-vertex) fit of the shape models to the scanning data was usually
validated. While this is a valuable parameter, it only gives a very limited indication of
25 the predictive capabilities of the models. Finally, despite the advent of head-centered
products such as EEG-recording devices [14], to the best of the authors' knowledge no
parametric models to date focus on the scalp.

In this work, a statistical 3D shape model of the human scalp is created and a linear
mapping is made between statistical parameters and ten anthropometric measurements.
30 The prediction accuracy of the model is examined by using three different error metrics,
i.e. vertex-to-vertex, normal and tangential error. Both the average and point-to-point
errors are evaluated for several combinations of anthropometric measurements. Cross-
validation is used to verify both the statistical and the anthropometric shape model. The
sensitivity the prediction to measurement errors for individual parameters is shown and

35 the effect of measurement errors on the prediction is evaluated. Such extensive analysis will allow ergonomists to select the minimal required set of anthropometric measurements, determine the influence of measurement errors and accurately locate shape variation.

The remainder of this paper is organized as follows. Section 2 describes how the
40 shape model is built, including the segmentation and parametrization of the MRI scans, the principal component analysis (PCA) of the 3D scalp geometry, the selection of the anthropometric measurements, and the correlation between these measurements and the PC weights. In section 3, the shape model is evaluated in terms of prediction accuracy, the data set size is verified for the statistical as well as the anthropometric model, and the
45 sensitivity of the prediction to measurement errors is discussed. The results are shown in section 4, as well a discussion on how to select the right anthropometric measurements and an application for anthropometric research and for industrial design. Finally, the conclusion is formulated in section 5.

2. Methods

50 This section presents the workflow of the methodology that was used to create the anthropometric shape model (see Fig. 1). Because the input MRI scans contain more information than just the skin surface, they first need to be preprocessed to remove all artefacts and to extract the cranium surface as a geometric surface mesh. This process is described in section 2.1.1. The surfaces then need to be aligned to each other and
55 be projected into a simpler parameter space for further analysis. This ensures that corresponding points are used throughout the remainder of the methodology, instead of possibly comparing e.g. the tip of the nose with the tip of the earlobe. Section 2.1.2 describes how this was done. The surfaces are then sampled so as to obtain a uniform set of corresponding points on which PCA can be performed to examine the shape variation,
60 as explained in section 2.1.3. However, as will be discussed in section 2.2.1, PCs are not intuitive enough to be used as parameters for the model. Therefore, section 2.2.2 concludes the methodology by showing how ten intuitive measurements can be used instead to analyze the head geometry and predict new head shapes.

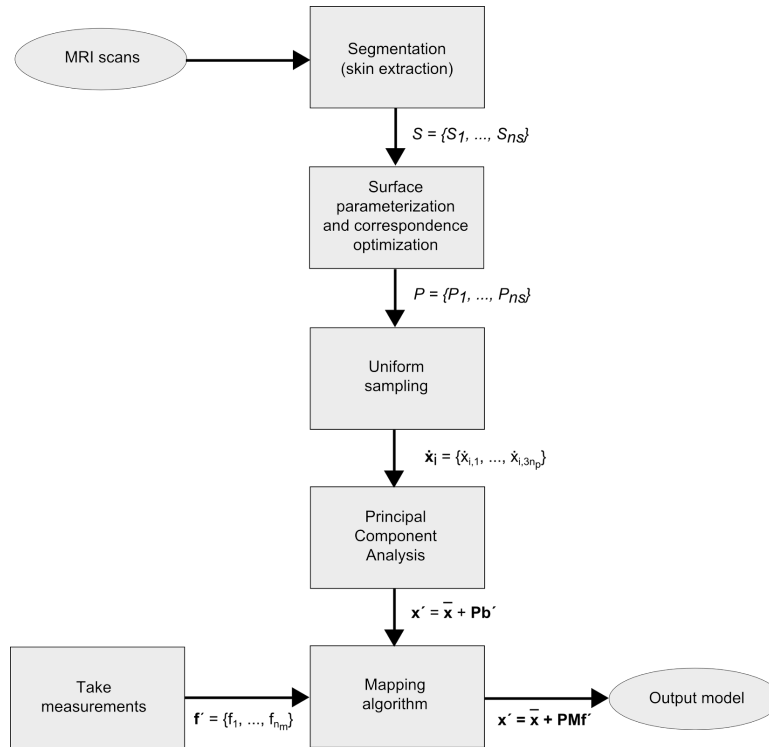


Figure 1: **Workflow.** The skin layer is first extracted from MRI scans, then the scalp surfaces are parameterized and corresponded to one another. After sampling the images using uniform landmark locations, PCA is performed on the resulting point cloud. Finally, the anthropometric measurements are acquired from the scalp surfaces and are correlated with the respective PC weights to create a mapping. This mapping results in an anthropometric model that can be used to predict new scalp surfaces based on anthropometric measurements.

2.1. Building the shape model

65 2.1.1. Segmentation of MRI Scans

100 MRI T1-FFE-weighted MRI scans (50 male, 50 female aged between 20 and 30 years, Western population) were used as input for the shape model. The scans were acquired using a Philips ACS III 1.5 T scanner in the sagittal acquisition plane, with a slice thickness of 1 mm, an echo time of 10 ms, a repetition time of 18 ms and a flip angle
70 of 30 degrees. These scans were obtained from the International Consortium for Brain Mapping (ICBM) database [15].

The first step in the processing pipeline was to segment the skin layer. Hereto, the MR images were debiased by Lloyd-Max quantization [16] and thresholded for grayscale intensity between 300 and 1800. Connected components labeling [17] was used to separate
75 the head from smaller noise artifacts and head fixation braces. Finally, a morphological closing operation was applied to fill cavities such as the ear canals and nostrils. The ensuing surface was then extracted using marching cubes [18] and any remaining holes were interpolated using Poisson surface reconstruction [19].

The skin surface of the cranium was extracted as the region of interest, because
80 the aim of this work was to mainly examine the variability of the scalp. To that end, each surface was cut by the shortest path connecting four consecutive points that were manually annotated on each surface: the subnasale (sn), both otobasia inferia (obi1 and obi2) and the inion (i) (see Fig. 2). The shortest path was determined using fast marching, in which a distance map is first calculated from the one boundary point to
85 the next, followed by gradient descent interpolation from the latter to former [20]. This resulted in a set of surfaces of the same topology $\mathcal{S} = \{\mathcal{S}_1, \dots, \mathcal{S}_{n_s}\}$, with n_s the number of surfaces.

2.1.2. Surface Parametrization and Correspondence Optimization

The next step was to correspond the 3D coordinate points of the surfaces to each other,
90 enabling statistical analysis of the 100 scans. The surfaces \mathcal{S} were mapped to a simpler parameter space by a process called surface parametrization. Many parametrization methods exist: if the corresponding surface is disc-like or spherical, a disc or sphere is often taken as the parameter space, while other domains are used for more complex

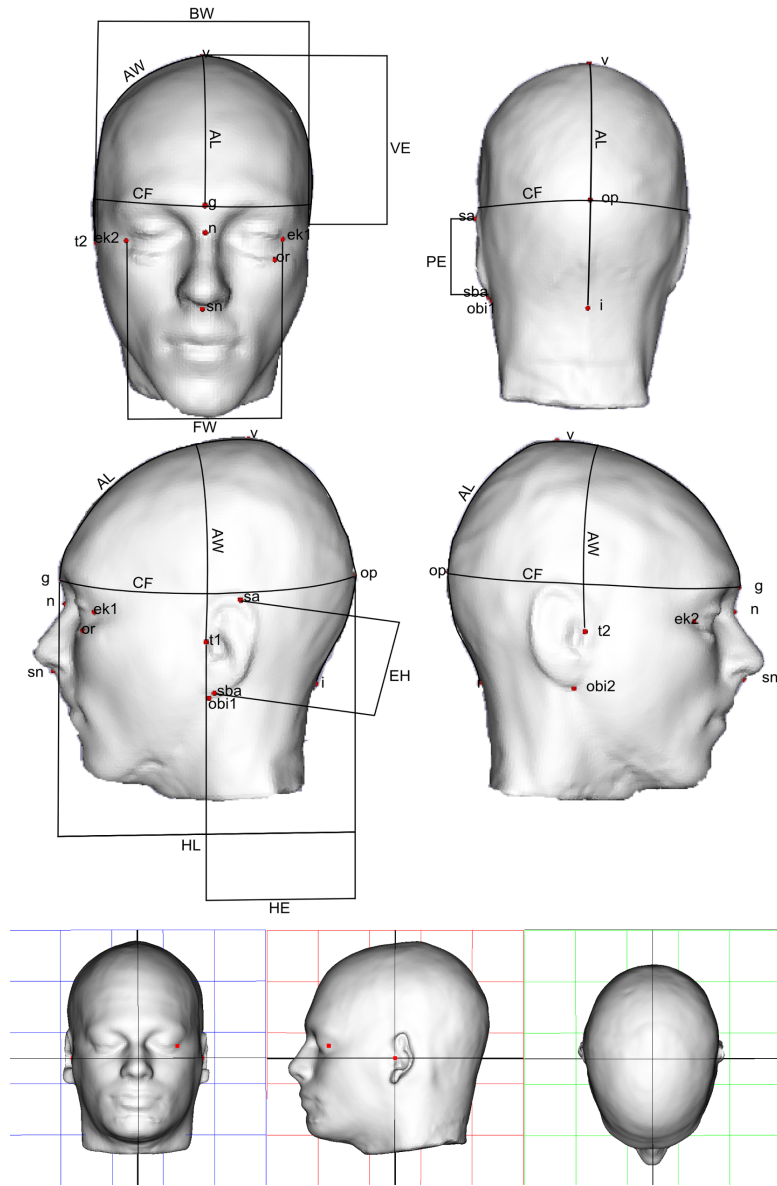


Figure 2: **Annotation points and coordinate system.** Anthropometric measurements and annotation points (top) and example of coordinate system used for anthropometric measurements showing the transversal (bottom left), midsagittal (bottom middle) and Frankfurt plane (bottom right), respectively, facing the front.

topologies [21]. In this paper, the approach of [21] was used, with the exception that the
95 head surfaces were mapped to a planer (two-dimensional) rectangle with sides of length
1. The set of parametrizations is $\mathcal{P} = \{\mathcal{P}_1, \dots, \mathcal{P}_{n_s}\}$; where \mathcal{P}_j is a parametrization for
a surface \mathcal{S}_j only if its nodes, edges and faces are embedded in the rectangular planar
domain and have a one-to-one correspondence to those of \mathcal{S}_j . The mapping $\phi : \mathcal{S} \rightarrow \mathcal{P}$
between the parameterizations \mathcal{P} and surfaces \mathcal{S} was calculated by defining each point in
100 \mathcal{P}_j as a linear combination of its neighbours [22]. The resulting system of linear equations
only has a unique solution if ϕ satisfies the Laplace equation $\Delta\phi = 0$ on the interior of
 \mathcal{S} . Once ϕ is defined on the boundary of \mathcal{S} , the system can be solved using finite element
analysis as in [23].

With the parameterizations well defined, point-to-point correspondence is the next
105 step. A group-wise correspondence optimization was performed [21], resulting in
high-quality correspondences and a compact model. This method consisted of two
steps: a rigid optimization in which the surfaces were aligned, and a non-rigid
optimization in which the parameterizations were locally deformed while the sur-
faces were kept optimally aligned, resulting in new parameterizations \mathcal{P} and trans-
110 formed surfaces \mathcal{S} . Fig. 3 shows the parametrization process and the corre-
spondence optimization in more detail. Since there are no points to correspond
below the boundary, the surfaces are aligned mainly according to the scalp re-
gion. The corresponded surfaces of all 100 scans used in this paper can be
downloaded from http://www.visielab.ua.ac.be/sites/default/files/research_
115 [topic_files/shape-matrix_29910-coordinates_x_100-surfaces_0.xlsx](http://www.visielab.ua.ac.be/sites/default/files/research_topic_files/shape-matrix_29910-coordinates_x_100-surfaces_0.xlsx).

2.1.3. Modeling the Shape of the Scalp

The corresponding parameterizations were used for statistical analysis of the under-
lying shapes. Each surface was sampled in the parameter space $\mathcal{P} \equiv [0, 1]^2$ with a
set of landmarks that resulted in a uniform distribution of landmarks over the aver-
120 age scalp. The 3D coordinates of these landmarks were concatenated into a vector
 $\dot{\mathbf{x}}_i = [\mathbf{v}_{i,1}, \dots, \mathbf{v}_{i,n_p}] = [x_{i,1}, y_{i,1}, z_{i,1}, \dots, x_{i,n_p}, y_{i,n_p}, z_{i,n_p}]$ with n_p the number of land-
marks. A $3n_p \times n_s$ shape matrix \mathbf{X} was then defined as $[\dot{\mathbf{x}}_1^T, \dots, \dot{\mathbf{x}}_{n_s}^T]$ (with n_s the number
of shapes) and zero-centered by subtracting the row-wise mean $\bar{\mathbf{x}}$ from each element for

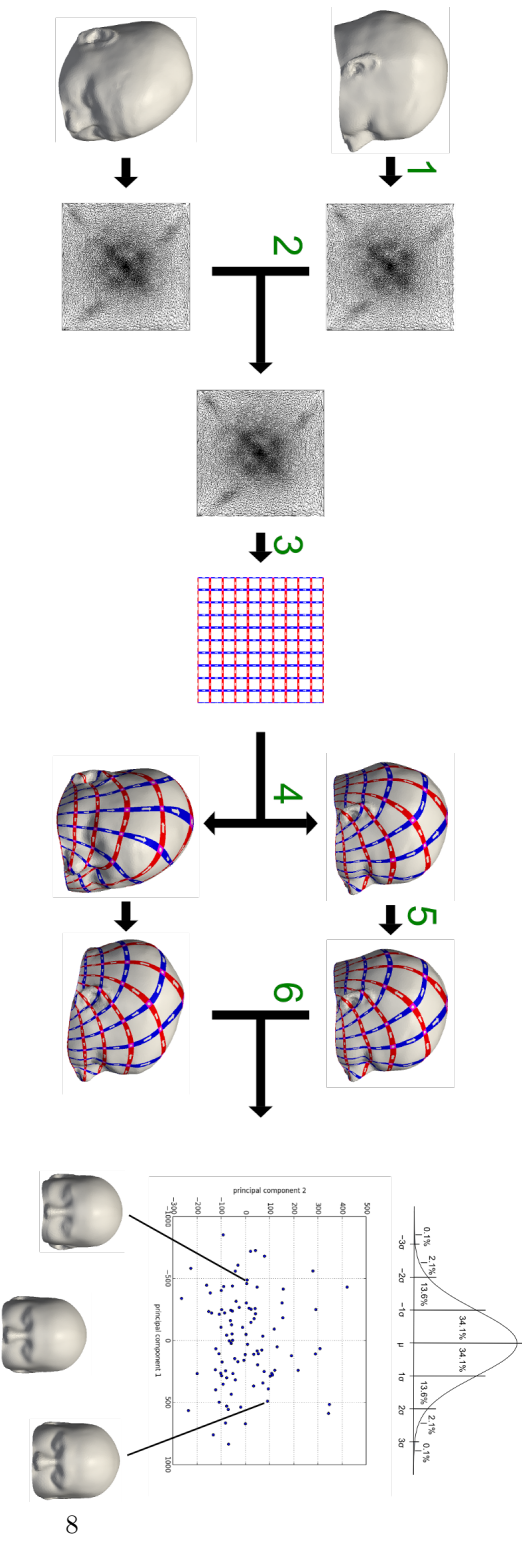


Figure 3: **Visualization of parametrization and correspondence optimization** First, all segmented surfaces are mapped onto a planar rectangle with sides of length 1 (step 1). The area distortion of the planar map is calculated for each surface and an average distortion map is derived in the rectangular domain (step 2). A dithering algorithm is performed on the average triangle area distortion, resulting in a resulting in a set of 10000 points that are approximately uniformly distributed over the surface of the scap (step 3). This grid is projected back on the original surfaces (step 4). The surfaces are translated, rotated and locally deformed in order to optimize the point correspondence to obtain a compact PCA model (step 5). This step ensures that equivalent anatomical landmarks on different surfaces, e.g. the tip of the nose or the earlobes, are closely located to each other in the planar parameterization domain. Without this step, resulting variations might be due to misalignment instead of actual shape variation. Finally, statistical analysis can be performed on the corresponding surfaces (step 6).

each respective surface:

$$\mathbf{X}_c = [\dot{\mathbf{x}}_1^T - \bar{\mathbf{x}}^T \dots \dot{\mathbf{x}}_{n_s}^T - \bar{\mathbf{x}}^T] \quad (1)$$

125 After applying PCA, each scalp can be represented as follows:

$$\mathbf{x}' = \bar{\mathbf{x}} + \sum_{j=1}^{n_s-1} \mathbf{P}_j \mathbf{b}'_j = \bar{\mathbf{x}} + \mathbf{P} \mathbf{b}' \quad (2)$$

where \mathbf{x}' is a column vector containing the vertex coordinates of the scalp, \mathbf{P} a $3n_p \times (n_s - 1)$ orthonormal matrix containing the principal component vectors as columns, and \mathbf{b}' a $(n_s - 1) \times 1$ column vector of weights of the respective PCs. By modifying the principal component weights \mathbf{b}' , new scalp surfaces can be constructed. Hence, Eq. 2
130 represents a shape model that is parametrized by the PC weights.

2.2. Extending the shape model with anthropometric measurements

2.2.1. Performing anthropometric measurements on the human scalp

The first five PCs are shown in Fig. 4. Unfortunately, PC weights do not provide an intuitive description of the shape of the scalp because the principal components have no
135 clear physical interpretation (e.g., 'volume' or 'size'). This leads to ambiguous definitions and clearly shows the need for a new set of intuitive parameters, i.e. anthropometric measurements. NEN-EN-ISO 7250.

Anthropometric measurements are usually defined according to standards which are based on the work of Rudolf Martin [24] in Europe, e.g. The measurements are taken
140 with respect to the Frankfurt plane, which is defined as the plane passing through the lower points of both eye sockets (in this work, the lowest point of the left eye socket (or) is used) and both tragia (t1 and t2) [25]. The other reference planes, the midsagittal and the transversal planes, are perpendicular to this plane (see Fig. 2).

The following measurements were selected (see Fig. 2):

145 *Head length (HL)*: glabella (g) to ophistokranion (op) distance.

Face width (FW): left ektokanthia (ek1) to right ektokanthia (ek2) distance.

Bitragion width (BW): left tragion (t1) to right tragion (t2) distance.

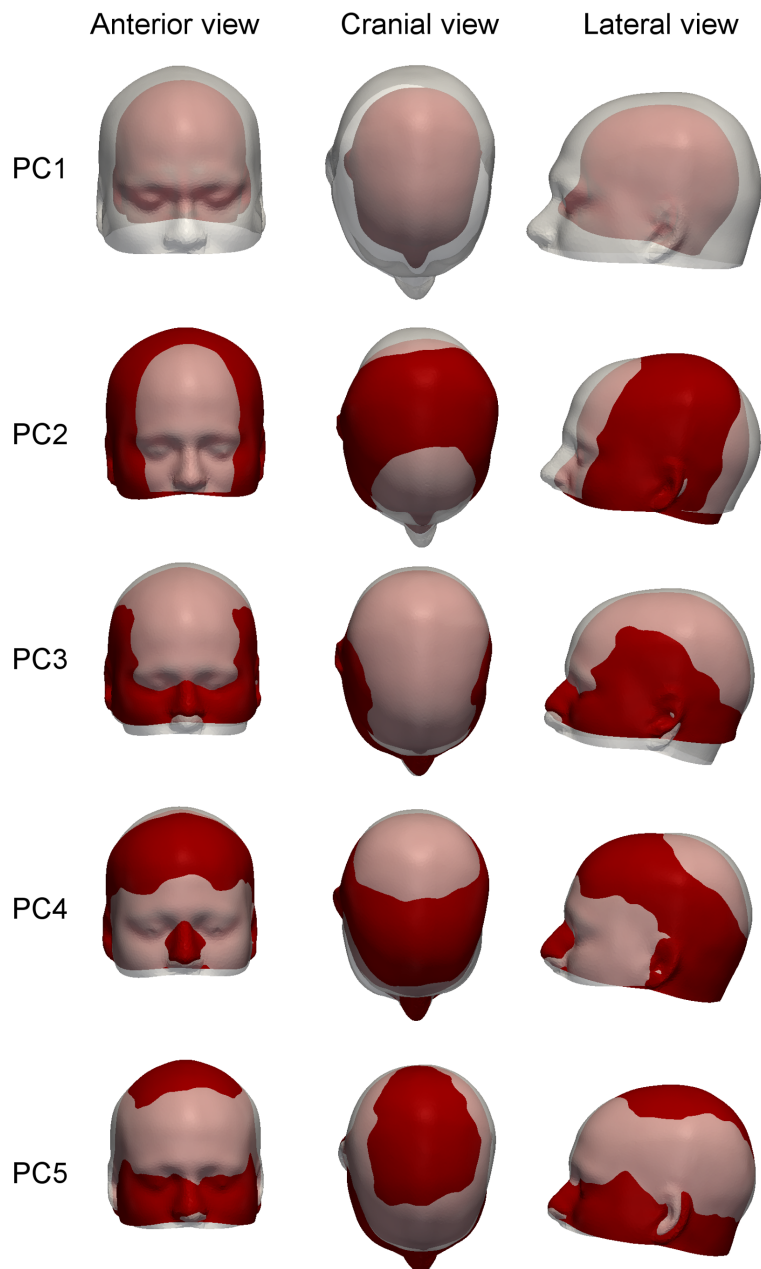


Figure 4: **Visualization of principal components.** Principal component 1 to 5 shown as the average head -3 (red) and +3 (white) standard deviations of the respective PC.

Ear height (EH): sub-aurale (sba) to super-aurale (sa) distance.

150 *Projected ear height (PE)*: sub-aurale (sba) to super-aurale (sa) distance, projected on the midsagittal plane.

Vertical position of the ear (VE): left trigion (t1) to vertex (v) distance, projected on midsagittal plane.

Horizontal position of the ear (HE): left trigion (t1) projected on midsagittal plane to ophistokranion (op) distance, projected on Frankfurt plane.

155 *Head circumference (CF)*: the length of the intersection of the head surface and the plane perpendicular to the midsagittal plane and going through the glabella (g) and ophistokranion (op).

Arc length (AL): measured over the surface of the head, from glabella (g) to inion (i) on the midsagittal plane.

160 *Arc width (AW)*: measured over the surface of the head, from trigion (t1) to trigion (t2) and perpendicular to the transversal plane (see below).

The measurements were performed on the input surfaces and concatenated into a vector $\mathbf{f}_i = [f_{i,1}, \dots, f_{i,n_m}]$ for each surface \mathcal{S}_i , with n_m the number of measurements, and combined into a $n_m \times n_s$ measurement matrix $\mathbf{F} = [\mathbf{f}_1^T, \dots, \mathbf{f}_{n_s}^T]$. The results of the measurements for the population head scans are summarized in Table 1. The full measurements for all 100 scans can be downloaded as a labeled spreadsheet from http://www.visielab.ua.ac.be/sites/default/files/research_topic_files/anthropometric_measurements_0.xlsx, and as the data matrix used throughout this work from http://www.visielab.ua.ac.be/sites/default/files/research_topic_files/feature-matrix_10-measurements_x_100-surfaces_0.xlsx.

2.2.2. Correlating anthropometric measurements and PCs

Next, the correlation between the anthropometric measurements and the PCs was studied. For this purpose, the multivariate regression approach of Allen et al. [3] was used. A linear method was chosen because it can be implemented using linear matrix operations, which are easy to calculate and allow for low delay dynamic interaction with

Table 1: Summary of anthropometric measurements

Measurement	<i>head length</i>	<i>face width</i>	<i>bitr. width</i>	<i>ear height</i>	<i>hor. pos. ear</i>
Max	222	108	167	70	114
Min	168	77	131	47	82
Mean	199	94	148	55	101
St. dev.	10.6	5.8	8.0	4.4	6.1
Measurement	<i>ver. pos. ear</i>	<i>proj. ear height</i>	<i>circ.</i>	<i>arc length</i>	<i>arc width</i>
Max	150	69	626	342	389
Min	109	47	511	262	298
Mean	133	55	565	304	346
St. dev.	7.2	4.4	25.7	16.5	17.5

Anthropometric measurements for a population of 100 individuals (50 male, 50 female, ages between 20 and 40).

the resulting shape model. An $(n_s - 1) \times (n_m + 1)$ mapping matrix \mathbf{M} was calculated as follows:

$$\mathbf{M} = \mathbf{B}\dot{\mathbf{F}}^+ \quad (3)$$

\mathbf{B} is a $(n_s - 1) \times n_s$ matrix containing the weight vectors corresponding to the measurements for each PC, as calculated in section 2.1.3. To account for y-intercepts in the regression, a row of ones was appended to the measurement matrix \mathbf{F} , represented as
180 $(n_m + 1) \times n_s$ matrix $\dot{\mathbf{F}}$, with pseudo-inverse $\dot{\mathbf{F}}^+$. For the purpose of this paper, $n_s = 100$, $n_p = 10000$ and $n_m = 10$. Once the mapping matrix was obtained, it was possible to calculate a weight vector \mathbf{b}' for a new set of measurements $\mathbf{f}' = [f'_1, \dots, f'_{n_m}, 1]$:

$$\mathbf{b}' = \mathbf{M}\mathbf{f}'^T \quad (4)$$

In order to create a new surface using custom anthropometric measurements, the
185 new \mathbf{b}' is simply inserted into Eq. (2) to obtain a new shape $\mathbf{x}' = [\mathbf{v}'_{i,1}, \dots, \mathbf{v}'_{i,n_p}] = [x'_{i,1}, y'_{i,1}, z'_{i,1}, \dots, z'_{i,3n_p}]$:

$$\mathbf{x}' = \bar{\mathbf{x}} + \mathbf{P}\mathbf{b}' = \bar{\mathbf{x}} + \mathbf{P}\mathbf{M}\mathbf{f}'^T \quad (5)$$

Thus, the shape model can now also be parametrized according to the anthropometric measurements and will be further referred to as the anthropometric model.

3. Experiments

190 In this section, the anthropometric shape model built in section 2 is evaluated. First, a number of error metrics are introduced in section 3.1.1 that will be used throughout the rest of the work to determine the accuracy of each prediction. The overall prediction quality is assessed in section 3.1.2, for anthropometric models built with single measurements or with combinations of them. In order to examine the generalization ability of
195 the models, cross-validation analysis is performed on the PCA model from section 2.1.3 and the anthropometric model from section 2.2.2 in sections 3.2.1 and 3.2.2, respectively. Finally, since errors due to human error or due to equipment properties sometimes occur

when measuring subjects, section 3.3 discusses the sensitivity of each of the anthropometric measurements to measurement errors.

200 3.1. Determining the distribution of the prediction errors

3.1.1. Prediction Quality Measures

To assess the accuracy of the prediction of a given shape model, three distance metrics were introduced: the geometric d_g , the normal d_n , and the tangential error d_t , between a point \mathbf{v} on the original surface and the corresponding point \mathbf{v}' on the mapped surface
 205 (see Fig. 5):

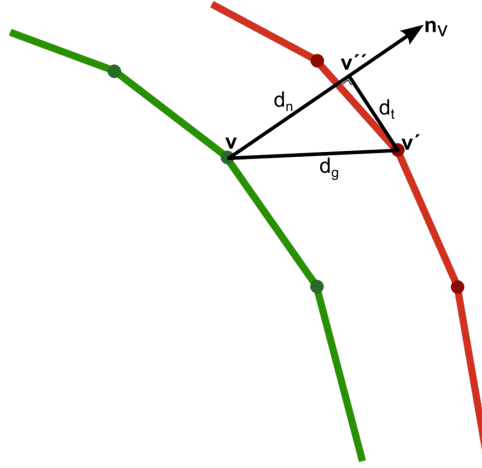


Figure 5: **Error metrics.** Visualizations of the error metrics used. The green line represents the original surface, the red line represents the prediction. Vertex \mathbf{v}' on the predicted surface corresponds to \mathbf{v} on the original surface. \mathbf{n}_v is the normal of vertex \mathbf{v} , and \mathbf{v}'' is the projection of \mathbf{v}' on \mathbf{n}_v . The geometric error between these points is the norm of vector $\mathbf{v}' - \mathbf{v}$, the normal error the norm of $\mathbf{v}'' - \mathbf{v}$ and the tangential error the norm of $\mathbf{v}'' - \mathbf{v}'$.

$$d_g(\mathbf{v}, \mathbf{v}') = |\mathbf{v} - \mathbf{v}'| \quad (6)$$

$$d_n(\mathbf{v}, \mathbf{v}') = |(\mathbf{v} - \mathbf{v}') \cdot \mathbf{n}_v| \quad (7)$$

$$d_t(\mathbf{v}, \mathbf{v}') = \sqrt{d_g(\mathbf{v}, \mathbf{v}')^2 - d_n(\mathbf{v}, \mathbf{v}')^2} \quad (8)$$

To assess the quality of a shape model prediction, the errors need to be combined

into a single meaningful number. To this end, the vertex errors are averaged into the shape geometric errors $D_g(\mathcal{S}_i)$ as follows:

$$D_g(\mathcal{S}_i) = \frac{1}{n_p} \sum_{\mathbf{v} \in \mathcal{S}_i} d_g(\mathbf{v}, \mathbf{v}') \quad \forall i = 1, \dots, n_s \quad (9)$$

Finally, the average of the shape geometric errors for a set of shapes \mathcal{S} is calculated
 210 for each mapping, resulting in the model geometric error $E_g(\mathcal{S})$:

$$E_g(\mathcal{S}) = \frac{1}{n_s} \sum_{\mathcal{S}_i \in \mathcal{S}} D_g(\mathcal{S}_i) \quad (10)$$

Furthermore, the error metrics were also calculated per point, resulting in a vector $\mathbf{e}_g = [e_g^{(1)}, \dots, e_g^{(n_p)}]$ of average point geometric errors, which can be used to visually locate the prediction errors of the model:

$$e_g^{(j)} = \frac{1}{n_s} \sum_{\mathcal{S}_i \in \mathcal{S}} d_g(\mathbf{v}_{i,j}, \mathbf{v}'_{i,j}) \quad \forall i = 1, \dots, n_s; j = 1, \dots, n_p; \mathbf{v}_i \in \mathcal{S}_i \quad (11)$$

Two approaches were considered for the calculation of the standard deviation. By
 215 taking the standard deviation over all $D_g(\mathcal{S}_i)$, one can gain insight on how the prediction errors vary across the entire population. The standard deviation over all vertex errors instead gives more information on the local error variation. The former was deemed to be of more use in evaluating the feasibility of a shape model for design purposes and was therefore used throughout most of this paper.

220 The model, shape, and point normal error $E_n(\mathcal{S})$ and tangential error $E_t(\mathcal{S})$ are calculated analogously.

3.1.2. Analysis of Anthropometric Model Prediction

Apart from the sensitivity for each anthropometric measurement, the prediction errors of the mapping using several combinations of measurements were also taken into
 225 account. First, an anthropometric shape model was built for the entire input population, using only one individual measurement to calculate the mapping (Eq. 3). The scalp shapes of the entire population (Eq. 4) were predicted with this mapping. Each of the 100 predicted shapes was calculated by creating a model using the 99 remaining shapes and predicting the shape based on the measurements. The average geometric, tangential

230 and normal errors 3.1.1 over all 100 scalp shapes were used to compare the prediction accuracy of each anthropometric measurement. In the same way, predictions were calculated for anthropometric models using all 1022 possible combinations of anthropometric measurements. This supports the creation of an anthropometric shape model with a minimal number of parameters.

235 3.2. Evaluating the data set size

3.2.1. Verification of PCA Model by Repeated Random Sub-sampling

To verify the robustness of the PCA model of section 2.1.3, repeated random sub-sampling was applied. Subsets of 10, 20, \dots , 90 scans were randomly selected from the 100 scans. PCA was performed on each subset (see section 2.1.3), resulting in a PC
240 matrix \mathbf{P}_t^T and an average surface $\bar{\mathbf{x}}_t$. One additional surface \mathbf{x}_v was randomly selected from the original data set (excluding the scans in the subset) to serve as validation data. The PC weights \mathbf{b}_v for \mathbf{x}_v were calculated as follows:

$$\mathbf{b}_v = \mathbf{P}_t^T (\mathbf{x}_v - \bar{\mathbf{x}}_t) \quad (12)$$

A new surface was then created by inserting the PC weights \mathbf{b}_v in Eq. (2). The resulting surface is a restriction of the original shape to the space spanned by the PCs
245 of the trained PCA model. The shape geometric errors (see section 3.1.1) between this restricted surface and the validation surface \mathbf{x}_v were then calculated. The above procedure was repeated for 1000 iterations. Finally, the average and standard deviation of all 1000 shape geometric errors were calculated for each of the subsets. Since the projection error contributes to the mapping error, it was important to ensure that it was
250 in the range of the original resolution of the MRI scans (1 mm).

3.2.2. Verification of Anthropometric Model by Repeated Random Sub-sampling

Next, the generalization ability of the anthropometric model using the mapping of section 2.2.2 was examined. This was done in a similar way to section 3.2.1, with the exception that a mapping was constructed between the PC weights and the measurements
255 using Eq. (3) of the training data. This mapping was then used to predict the shape of a randomly selected scalp surface (excluded from the training data). The geometric error

between the predicted surface and the original surface was used to assess the robustness of the mapping.

3.3. Sensitivity Analysis of Mapping Algorithm

260 The prediction error of the anthropometric model is influenced by the skills of the practitioner [26, 27], the precision of the equipment and the measurement method (direct measurement, measurement from 2D images or from 3D images) [28]. Therefore, the sensitivity of the prediction to measurement errors ought to be examined. In this section, a distinction is made between the anthropometric measurement (e.g. *head length*) and
265 the measurement value (e.g. 190 mm). In order to obtain a single factor to express the sensitivity for each anthropometric measurement, a Monte Carlo analysis was performed on a full anthropometric model. Assuming that physical measurement errors follow a normal distribution, a range of normally distributed errors were added to the value of each anthropometric measurement, and a number of surfaces was predicted using the
270 aberrated measurements. The prediction errors for these surfaces were averaged over 1000 trials for each step in the error range and a regression line was fitted to the averages and standard deviations.

4. Results and Discussion

In this section, the results are shown. First, the data set size and region of interest
275 are discussed in section 4.1. A quantitative and qualitative analysis of the shape model is made in section 4.2, and the selection of the right anthropometric models for a desired prediction accuracy is discussed. Two applications are discussed at the end of the chapter, section 4.3 demonstrates a comparison between the male and female head shape, section 4.4 explores the design of the brain-computer interface using an anthropometric shape
280 model.

4.1. Data Set and ROI Selection

4.1.1. Discussion on the data set size

A data set of MRI scans was used as input because of several reasons. Firstly, the high availability of MRI data, e.g. in university hospitals, eliminates the need for volunteer

285 recruitment and time-consuming scanning sessions. As opposed to CT, MRI does not
operate with ionizing fields [29]. Furthermore, extracting the skin layer directly means
that there is no image occlusion due to hair. If necessary, the hair could be modeled
separately. Alternatively, one might want to examine the effect of ethnicity, e.g. by
considering scans from the Chinese population [30]. As long as the data can be extracted
290 as a polygon surface, the presented methodology can be extended to other input data
sets.

4.1.2. Verification of PCA Model and Anthropometric Model

Fig. 6 (left) shows the average and standard deviation of the geometric error for the
PCA model, as defined in section 3.2.1. The geometric error levels at 0.64 ± 0.12 mm for
295 100 shapes, indicating a proper approximation (around 1 mm) of the head shape for the
given population. Furthermore, the fact that there is a linear correlation between the PCs
and the anthropometric measurements is supported by the outcome of the procedure in
section 3.2.2: when using the anthropometric shape model for prediction, the geometric
error again levels for 100 shapes, this time at 1.52 ± 0.37 mm. The results are plotted in
300 Fig. 6 (right).

4.2. Selecting an appropriate shape model

4.2.1. Applying the error metrics

The three error metrics provide distinctly different information that benefits the in-
terpretation of the prediction. The geometric error d_g is the most obvious one, and is
305 commonly used in geometric modeling to determine the linear distance between a original
and a predicted point. As such, it offers information on the spatial location of points in
the prediction. In general, the higher this distance, the worse the prediction is consid-
ered to be. However, it contains no information on the direction in which the point has
moved between predictions. The normal error d_n , on the other hand, shows whether the
310 predicted point has moved towards the inside or outside of the shape. This knowledge
is useful for fixation purposes: a higher normal error means that it is uncertain whether
the retention system system (e.g. a hinge or a spring system) will be able to provide
the right amount of flexibility. A designer will then either have to choose other fixation
regions or another anthropometric model. Finally, the tangential error d_e expresses how

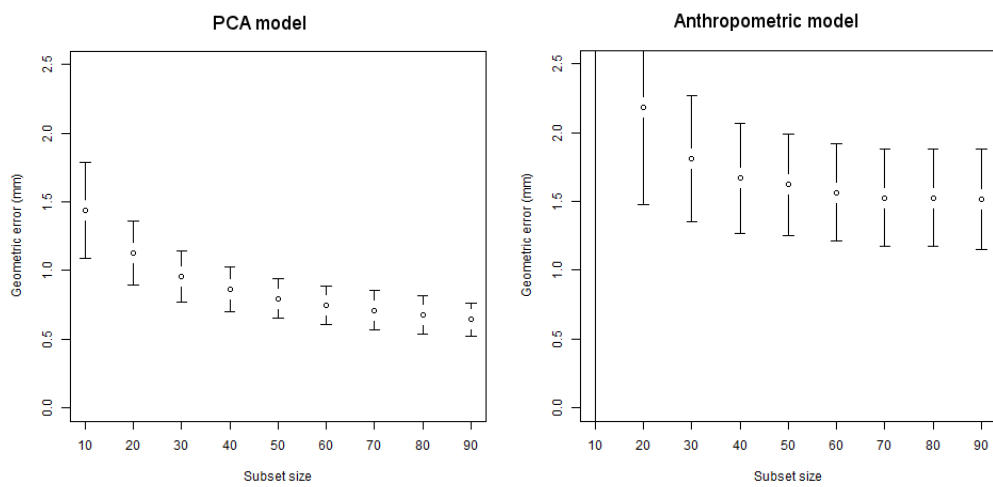


Figure 6: **Verification of PCA model and anthropometric model.** Average geometric error per subset size for shape model under repeated random sub-sampling and for 1000 iterations. Left: verification of PCA model with the first geometric error 1.44 ± 0.35 mm (subset of 10 shapes) and the last one 0.64 ± 0.12 mm (subset of 90 shapes). Right: verification for anthropometric measurement model with the first geometric error (out of range in the plot) 18.6 ± 27.5 mm (subset of 10 shapes), and the last one 1.52 ± 0.37 mm (subset of 90 shapes).

315 much the point has moved along the surface of the shape. The higher this number, the
larger the contact area between a product and the head will have to be. If it is too high,
this requirement might result in overlapping contact areas. This is problematic for sensor
application, e.g. for EEG-electrodes. The three measures combined provide information
for a wide range of applications and can be used both to evaluate the feasibility of a
320 given shape model and to assist in the determination of product specifications.

4.2.2. Quantitative Analysis of the Anthropometric model

As discussed in sections 1 and 2.2.1, there is a clear need for a shape model
parametrized by simple, intuitive parameters when head product design is envisaged.
The prediction errors (see section 3.1.1) for individual measurements are summarized
325 in Table 2, the errors for various combinations in Table 3. The required number and
combination of measurements will depend on the intended application. For example, if
a geometric error of no more than 2.5 ± 0.1 mm on average is acceptable, one might
use the *head length*, *circumference* or *bitragion width* individually to predict the three
dimensional shape of a customer's head and create a 3D design.

330 Sometimes, an ergonomist will only have a limited set of physical measuring tools
(e.g. calipers) at hand. In these cases, using a subset measurements would be preferred
to finding the tools necessary to acquire all measurements. However, this advantage
comes at a price: the average geometric prediction errors increase to 1.80 ± 0.47 mm, as
shown in Table 4 and 7.

335 If the prediction error should be lower (e.g. for personalized EEG devices), more
anthropometric measurements will be required, as shown in Table 3. A surprising fact
from this table is that the best prediction, with a geometric error of 1.38 ± 0.27 mm, a
normal error 1.27 ± 0.26 mm, and a tangential error 0.15 ± 0.03 mm is achieved by using
eight measurements, leaving out *ear height* and *projected ear height*. As of yet, it is not
340 clear whether this is due to the segmentation process or because the anthropometry of
the ear is actually not related to that of the head. Therefore, the current dataset cannot
be used for designs that rely on detailed description of the ear geometry.

Another parameter to consider is the desired percentage of the population that the
model should cover for a selected prediction error. This can be visualized by plotting the
345 cumulative distribution function (CDF), as in Fig. 7. For example, while the combination

Table 2: **Average prediction errors for individual anthropometric measurements**

Measurement	geom. error (E_g^S)	norm. error (E_n^S)	tan. error (E_t^S)
<i>all</i>	1.61 ± 0.36	1.40 ± 0.32	0.20 ± 0.03
<i>head length</i>	2.32 ± 0.94	2.04 ± 0.84	0.21 ± 0.03
<i>face width</i>	3.06 ± 1.41	2.74 ± 1.30	0.21 ± 0.03
<i>bitrignon width</i>	2.46 ± 0.99	2.17 ± 0.90	0.21 ± 0.03
<i>ear heigh</i>	3.28 ± 1.65	2.97 ± 1.53	0.21 ± 0.03
<i>hor. pos. ear</i>	2.90 ± 1.20	2.60 ± 1.10	0.21 ± 0.03
<i>ver. pos. ear</i>	2.64 ± 1.06	2.40 ± 0.99	0.19 ± 0.02
<i>proj. ear height</i>	3.26 ± 1.63	2.94 ± 1.51	0.21 ± 0.03
<i>circumference</i>	2.03 ± 0.68	1.78 ± 0.61	0.21 ± 0.03
<i>arc length</i>	2.60 ± 0.95	2.33 ± 0.89	0.20 ± 0.03
<i>arc width</i>	2.64 ± 1.03	2.39 ± 0.96	0.20 ± 0.03

Model average geometric, normal and tangential error for shapes predicted by the shape model using individual measurements (expressed in mm) for each shape in the data set (i.e. 100 shapes for this experiment).

Table 3: Average prediction errors for combinations of anthropometric measurements

Measurement	geom. error (E_g^S)	norm. error (E_n^S)	tan. error (E_t^S)
<i>HL, FW, BW, HE, VE, PE, CF, AL, AW</i>	1.60 ± 0.36	1.40 ± 0.31	0.20 ± 0.03
<i>HL, FW, BW, HE, VE, CF, AL, AW</i>	1.60 ± 0.35	1.40 ± 0.30	0.20 ± 0.03
<i>HL, FW, BW, EH, CF, AL, AW</i>	1.63 ± 0.37	1.43 ± 0.30	0.20 ± 0.03
<i>HL, FW, BW, CF, AL, AW</i>	1.63 ± 0.36	1.42 ± 0.30	0.20 ± 0.03
<i>HL, BW, CF, AL, AW</i>	1.63 ± 0.37	1.43 ± 0.31	0.20 ± 0.03
<i>HL, BW, CF, AW</i>	1.64 ± 0.39	1.43 ± 0.32	0.20 ± 0.03
<i>HL, CF, AW</i>	1.70 ± 0.45	1.49 ± 0.39	0.20 ± 0.03
<i>HL, CF</i>	1.80 ± 0.52	1.54 ± 0.44	0.21 ± 0.04

Average geometric, normal and tangential error for shapes predicted by the anthropometric model using combinations of measurements, expressed in mm. HL = head length, FW = face width, BW = bitragion width, EH = ear height, HE = horizontal position of ear, VE = vertical position of ear, PE = projected ear height, CF = circumference, AL = arc length and AW = arc width.

Table 4: Average prediction errors for optimal combinations of anthropometric measurements for different tools

Tool	Meas.	geom. error (E_g^S)	norm. error (E_n^S)	tan. error (E_t^S)
calipers	<i>HL, FW, BW</i>	1.86 ± 0.47	1.58 ± 0.37	0.22 ± 0.04
calipers	<i>HL, BW</i>	1.88 ± 0.50	1.61 ± 0.40	0.21 ± 0.04
tape measure	<i>CF, AL, AW</i>	1.84 ± 0.49	1.63 ± 0.44	0.19 ± 0.03
tape measure	<i>CF, AW</i>	1.87 ± 0.52	1.66 ± 0.46	0.19 ± 0.03

Average geometric, normal and tangential error for shapes predicted by the anthropometric model using combinations of measurements that can be measured using a single tool, expressed in mm. HL = *head length*, FW = *face width*, BW = *bitragion width*, CF = *circumference*, AL = *arc length* and AW = *arc width*.

of *head length* and *bitracion width* offers an average geometric error of 1.88 ± 0.50 mm, Fig 7 (top left) shows that less than 70 percent of the population will actually have a geometric error lower than 2 mm. This might suffice for designs which aim to incorporate a higher amount of customizability, but it will not be enough for highly personalized products with fewer customization options. In the latter case, a combinations covering a higher percentage will be preferred, e.g. *head length*, *bitracion width*, *circumference*, *arc length* and *arc width* (80 percent, see Fig. 7, top right).

Finally, the sensitivity of the anthropometric model to measurement errors, as explained in section 3.3, should be taken into account. The results of the regression on prediction errors induced by measurement errors are listed in Table 5. Multiplying the slopes of these lines with an expected measurement error provides an estimate of the geometric error and standard deviation of the resulting shape model. While the *head length* and *circumference* both yield the very low individual prediction errors, *head length* is also more sensitive to measurement errors than *circumference*. Because the mapping was created using digital measurements, errors for measurements from digital surfaces will be smaller than those from physical measurements with calipers and measuring tapes. In this case, the sensitivity will be a less influential factor and a small number of anthropometric measurements can be used to build the anthropometric model (e.g. *head length* and *bitracion width*). In contrast, when performing physical measurements, it is advisable to include anthropometric measurements with lower sensitivity and lower geometric errors in the anthropometric model (e.g. *circumference*, *arc length* and *arc width*). Again, *ear height* and *projected ear height* seem to be the most sensitive. Seeing as they also offer the worst individual prediction errors, the authors do not recommend using these as parameters for scalp-based designs.

4.2.3. Qualitative Analysis of Anthropometric Model

The average point geometric errors for all 100 predicted shapes are shown as a color map on the average head shape in Fig. 8. The figure shows the errors for the model using all measurements and for several combinations. The predictions on the forehead and the temporal regions seem to degrade when using less anthropometric measurements, which is especially clear for the combination of *head length* and *bitracion width*. The error metrics give a rough indication of the direction and magnitude of the prediction errors. The color

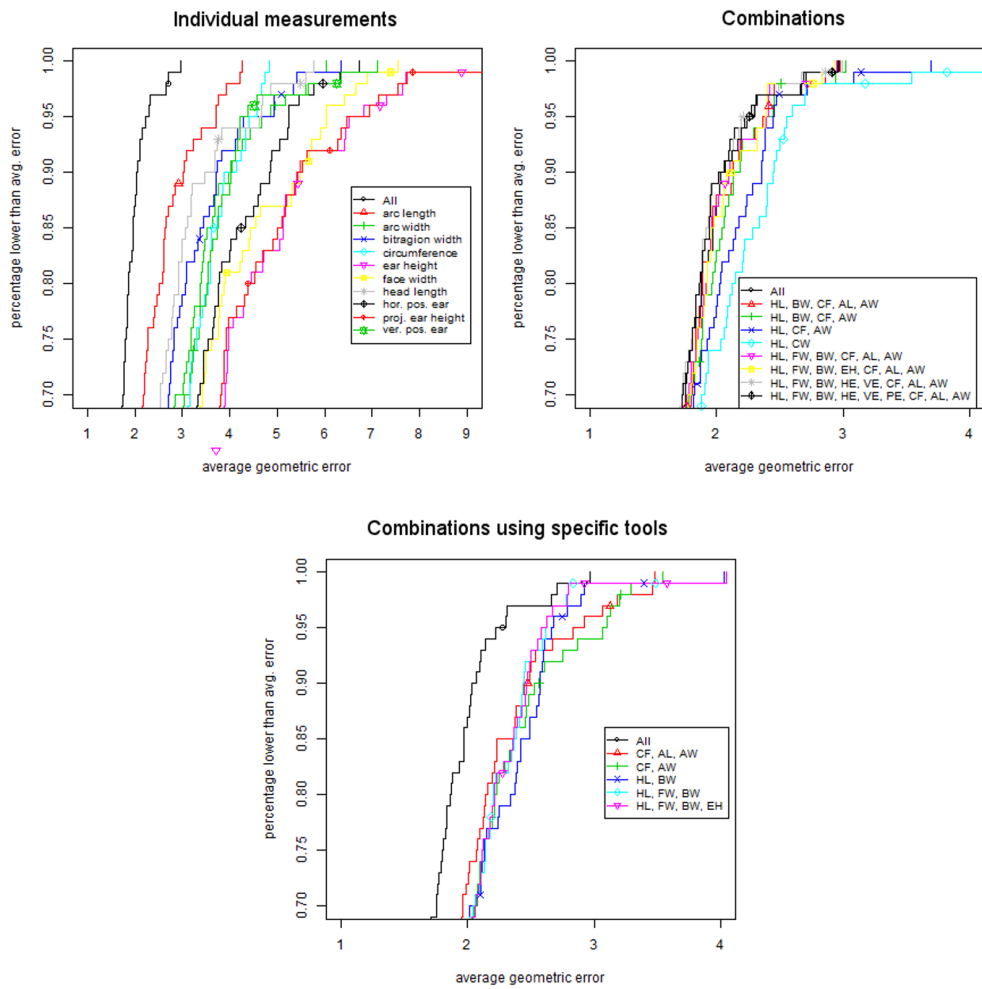


Figure 7: **CDF of average geometric error.** Cumulative distribution of average geometric error for an anthropometric model built using individual measurements (top left), combinations of measurements (top right), and combinations using specific anthropometric tools (bottom), including a full anthropometric model for comparison.

Table 5: **Sensitivity of the prediction to measurement errors**

Measurement	geom. error slope	Geom. st. dev. slope
<i>head length</i>	0.14	0.11
<i>face width</i>	0.04	0.03
<i>bitracion width</i>	0.09	0.07
<i>ear heigh</i>	0.47	0.36
<i>hor. pos. ear</i>	0.06	0.05
<i>ver. pos. ear</i>	0.12	0.09
<i>proj. ear height</i>	0.50	0.38
<i>circumference</i>	0.07	0.05
<i>arc length</i>	0.02	0.02
<i>arc width</i>	0.05	0.04

Slope of the regression line through the average geometric error and standard deviation for a Monte Carlo analysis performed for 1000 trials using the anthropometric model with all measurements. For anthropometric models using measurements with high slopes, measurement errors will have a larger impact on the resulting shape prediction.

map makes it possible to locate the measurement errors and to inform ergonomists which areas need extra attention and testing. For example, areas with a low normal error allow for product parts that fit closely to the skin, while areas with a high normal error might
380 need additional cushioning.

The high errors at the boundary result from the fact that the surfaces are aligned using the corresponding points in the upper region of the head and more variation is expected at the lower side, as explained in section 2.1.2. Because the region of interest of the scalp, the bias is acceptable.

385 Fig. 9 shows some examples of shapes resulting from the mapping using all measurements. As long as the input range stays within three standard deviations of the mapped PC weights, realistic head shapes can be obtained. The variability of the underlying shapes can be visualized according to the tensor Frobenius norm of the landmark covariance matrix [31]. A color map of this norm overlaid on the average head shape is shown
390 in Fig. 10.

4.3. Application for anthropometric research: comparison of male and female population

For this application, separate shape models were created for the male and female subgroups of the sample. The distribution of the PC weights for the entire population were separated into male and female subsets and statistically compared to find out which
395 ones differ the most between the groups. The anthropometric measurements were also compared to discover which ones are best suited for characterizing male and female head shapes. A summary of the anthropometric measurements for the male and female parts of the population are shown in Table 6.

Table 7 shows that the most significantly different measurements (according to the
400 Welch's t-test) are *head length*, *bitracion width* and *circumference*, which also offer the lowest individual prediction errors.

The first principal component seems to be the most significant one, see Table 8. This is supported by Fig. 11, where the average male and average female head are depicted, together with the distance between the respective shapes. For the sample means, the
405 overall size of the clearly head seems to vary, which indeed corresponds to the first PC (see Fig. 4). Furthermore, the distance between the shapes seems to be the highest on

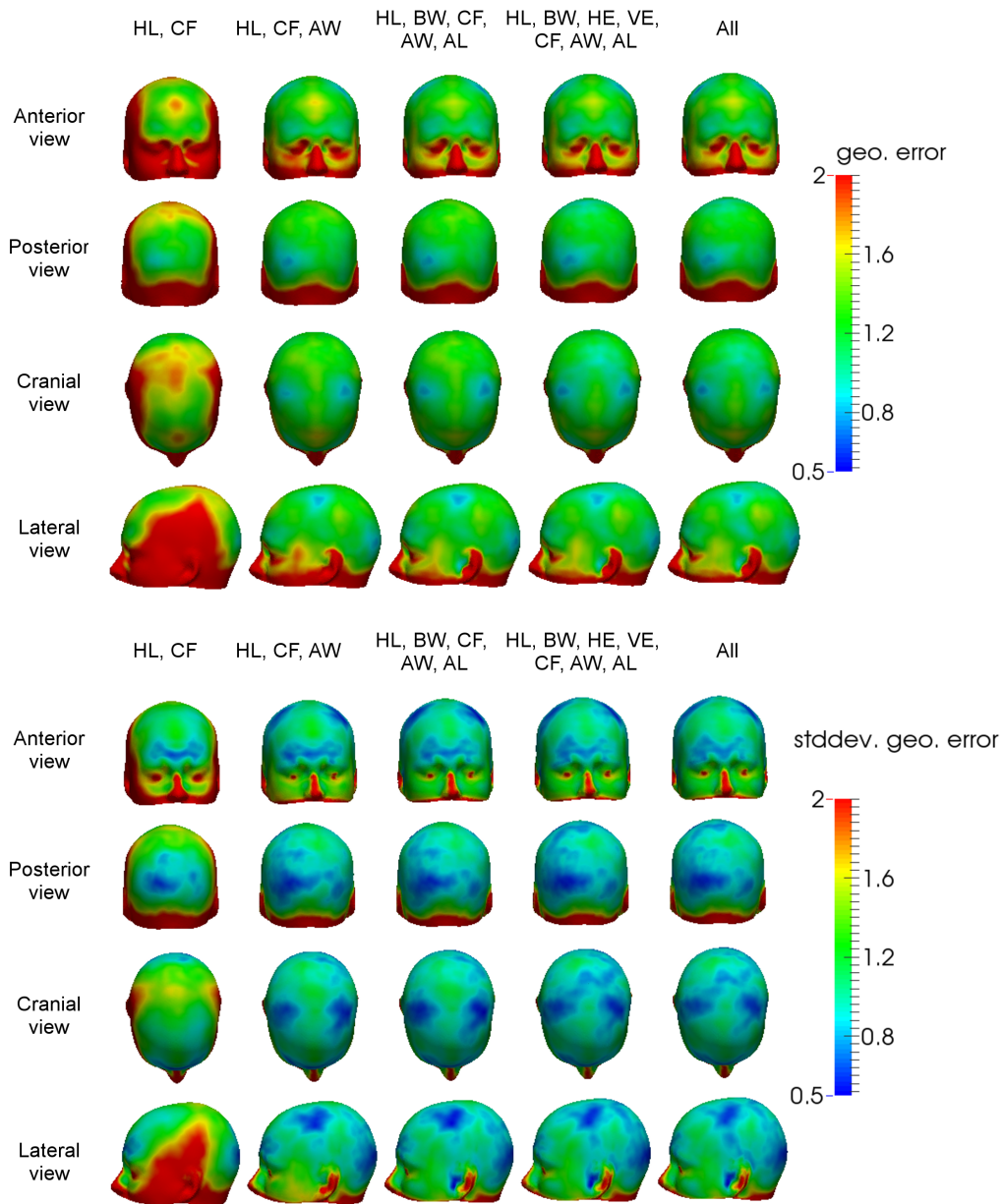


Figure 8: **Color map of geometric errors.** Average geometric error per point (top) and standard deviation of the geometric error (bottom) for the anthropometric measurement mapping in mm, shown on a 3D surface representing the average head for the model created with models using different combinations of anthropometric measurements. HL = head length, FW = face width, BW = bitrignon width, CF = circumference, AL = arc length, AW = arc width.

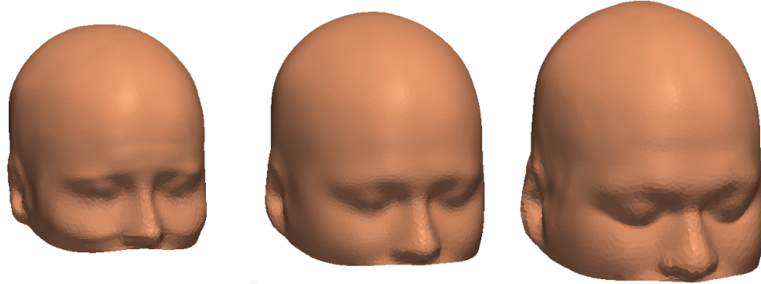


Figure 9: **Example surfaces generated using the anthropometric model.**

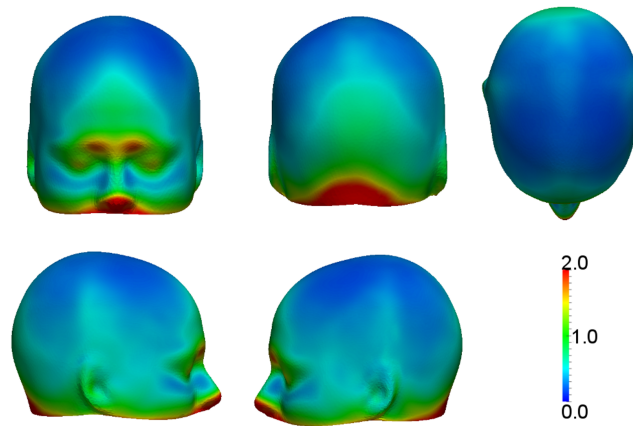


Figure 10: **Variability of the human scalp.** Variability of the scalp shape shown on the average 3D surface, expressed in terms of landmark covariance matrix Frobenius norm (in mm). High-variability regions are shown in red; low-variability regions are shown in blue.

Table 6: **Summary and significance of anthropometric measurements**

Meas.	<i>head length</i>	<i>face width</i>	<i>bitr. width</i>	<i>ear height</i>	<i>hor. pos. ear</i>
Male avg.	206 ± 7.9	96 ± 5.7	153 ± 6.3	57 ± 4.6	103 ± 5.2
F avg.	191 ± 7.4	92 ± 5.1	142 ± 5.2	53 ± 2.8	98 ± 5.8
p	1.26E-15	2.97E-04	1.47E-15	1.60E-07	2.97E-06

Meas.	<i>ver. pos. ear</i>	<i>proj. ear height</i>	<i>circ.</i>	<i>arc length</i>	<i>arc width</i>
Male avg.	137 ± 5.7	57 ± 4.6	584 ± 18.3	315 ± 13.0	356 ± 13.1
F avg.	129 ± 6.5	52 ± 2.7	546 ± 16.1	293 ± 11.3	337 ± 16.5
p	2.83E-08	3.14E-08	2.20E-16	1.32E-14	1.95E-08

Average anthropometric measurements for male (M) and female (F) population. The t-, df- and p-values for a Welch's t-test between both populations is also included. Only the measurements with p-value <0.05 are significantly different for the male and female populations.

Table 7: **Average prediction errors for male and female population**

Measurement	Geom. error (E_g^S)	Norm. error (E_n^S)	Tan. error (E_t^S)
Mixed	1.59 ± 0.50	1.36 ± 0.43	0.21 ± 0.03
Mixed to F	1.82 ± 0.47	1.59 ± 0.43	0.21 ± 0.03
F to F	1.62 ± 0.34	1.42 ± 0.32	0.20 ± 0.03
Mixed to M	1.89 ± 0.47	1.65 ± 0.43	0.21 ± 0.03
M to M	1.71 ± 0.38	1.49 ± 0.33	0.20 ± 0.03

Average geometric, normal and tangential error for prediction of the male and female population using various shape models. Mixed gender is a model containing 25 female and 25 male scalp shapes, F contains 50 female scalp shapes and M contains 50 male scalp shapes.

the forehead, above the eyebrows. (As explained in section 4.2.3, the higher error at the boundary is due to the correspondence algorithm.)

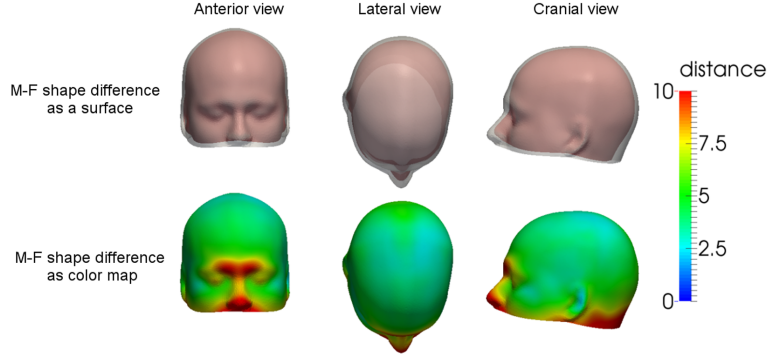


Figure 11: **Difference between male and female head.** The top row shows the difference between the average shapes of the male (white, transparent) and female (red) head. The bottom row shows the distance per point (in mm) as a color map on the average male head.

Table 8: **Significance of principal components**

Statistic	PC1	PC2	PC3	PC4	PC5
p	6.89E-15	0.306	0.187	0.017	0.269
Statistic	PC6	PC7	PC8	PC9	PC10
p	0.068	0.254	0.992	0.257	0.232

Significance of the first then PCs, determined using a Mann Whitney U-test. U- and p-value is shown for each of the PCs. Only PCs with p-value <0.05 are significantly different for the male and female population.

After this, the prediction errors for both models were first calculated separately as
 410 in section 3.1.2. Because using the full shape model of 100 shapes to predict the 50
 male or female shapes would inevitably result in a better comparison, 25 male and 25
 female scans were randomly removed from the full shape model to create a mixed gender
 shape model. The mixed gender model was used to predict the remaining 25 male and 25
 female shapes. This procedure was then repeated using the latter shapes as training data
 415 and the former ones for validation. The resulting predictions errors were then averaged.

Finally, the predictions of the male shapes by a completely female shape model and the predictions of the female shapes by a male model were also calculated for comparison.

The results of the shape predictions are shown in Fig. 12 and Fig. 13. As expected, the prediction of the male shapes by the male models offers a lower geometric error (1.71 ± 0.34 mm) than the prediction of the male shapes by the mixed model (1.89 ± 0.47 mm), and the prediction of the female shapes by the female model a lower one (1.62 ± 0.34 mm) than that of the female shapes by the mixed model (1.82 ± 0.47 mm). Furthermore, Fig. 12 and Fig. 13 show that when using a mixed model to predict either gender, most of the errors are concentrated at the eyebrow ridge, around the glabella.

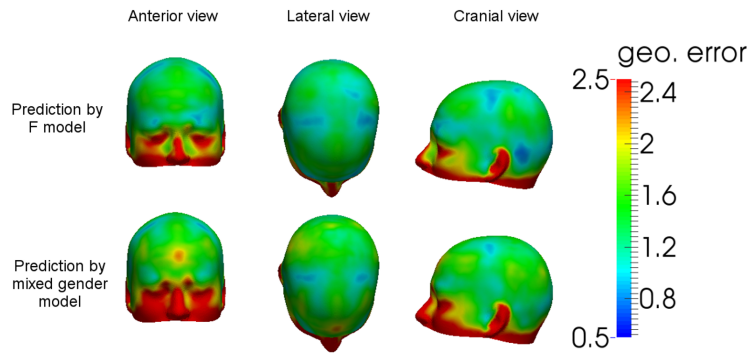


Figure 12: **Prediction error for female shapes.** Average point geometric errors for predictions of 50 female scalp shapes by a model consisting of 50 female shapes and a mixed model consisting of 25 female and 25 male shapes.

The observations in this chapter support earlier literature that concludes male and female head shape differ mostly in overall size [32] and in the size of supraorbital ridge [33, 34]. The same analysis could be performed to compare subsets of different ages and ethnicities. Unfortunately, the current data set does not contain information on the ethnicity of the subjects.

4.4. Application for industrial design: design of a brain-computer interface

In this chapter, an application of the model for industrial design will be discussed. One product that would benefit from design using anthropometric shape models, is an EEG-monitoring headset for Brain-Computer Interfacing (BCI) [35]. One of the main

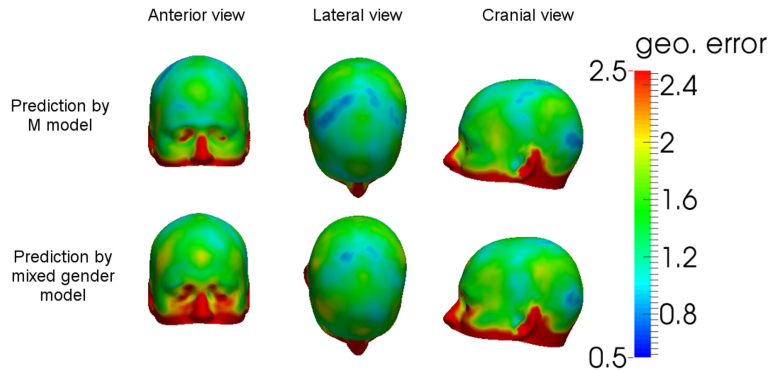


Figure 13: **Prediction error for male shapes.** Average point geometric errors for predictions of 50 male scalp shapes by a model consisting of 50 male shapes and a mixed gender model consisting of 25 female and 25 male shapes.

challenges in BCI design is creating an EEG-monitor that is at the same time comfortable,
 435 easy to use, and accurate. These requirements can only be met if designers can properly
 accommodate for the variability of the head. An anthropometric shape model can be used
 to achieve the desired level of accuracy. To demonstrate this, a prototype headset was
 created using a custom plugin for SolidWorks [36]. This plugin allows importing a shape
 model as a B-spline surface and parametrizing it according to a number of anthropometric
 440 features [37]. Certain points of a CAD design can be linked to parametric head and will
 automatically adapt when its dimensions are changed.

To create the BCI headset, the designer will first need to determine what the product
 should look like and how it should be fixated on the head. For instance, people generally
 do not prefer pressure on the temporal regions. Thus, a retention system that puts
 445 pressure on the frontal and occipital regions of the scalp is ideal. Using the color maps
 in Fig. 8, he can determine if a given shape model offers an accurate prediction on these
 region of interest. For this purpose, he needs to know how much error is acceptable on
 individual predictions. Say the customer is paralysed and wishes to use a BCI for assisted
 communication. Seeing as the patient will wear the headset for extended periods of time,
 450 the comfort and the fit are very important. In this case, the lowest possible prediction
 error will need to be achieved. As discussed in the paper, the lowest prediction error
 occurs for shape models parametrized by all of the measurements minus the *ear length*

and *projected ear length*. While it will take some time to perform the remaining eight measurements, this process will only need to be performed once and thus speed is not as important as accuracy. The designer then predicts the user's individual head shape
455 using the shape model and design a product using the head shape as a mannequin. An example of such a product is shown in Fig. 14 for three different shape predictions, with electrodes at locations Fpz1, Fpz2 and Oz according to the international 10-20 system [38]. While the shape of the headset is changed according to each individual prediction,
460 the electrodes will remain at the proper positions. This is due to the fact that the electrode contact points have been linked with the shape model. The designer therefore does not have to realign the design for each new user. Instead, he has only to adapt the curvature of the headset's upper brace. Depending on the prediction error derived from Table 3, an extra layer of cushioning can be added to this product in order to ensure
465 optimal fit and comfort.

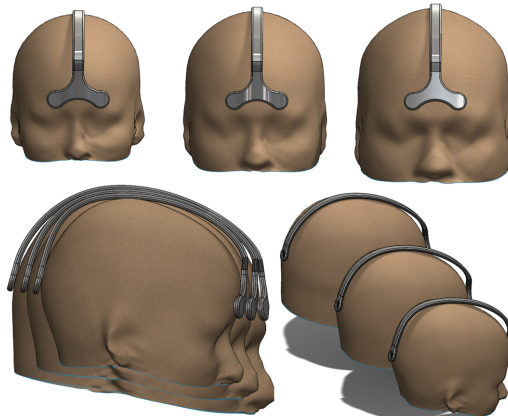


Figure 14: Example of an individualized brain-computer interface headset created with the anthropometric shape model.

Alternatively, a BCI headset might be required by a research lab in order to prototype BCI-software. In this case, a more generic product is preferable. The designer now needs to create an adjustable headset, using as few parameters as possible to predict the optimal size of the head. Based on the results in Table 2 and Table 3, the designer selects *head*
470 *length* and *circumference* as parameters. Comfort or fit is not as important in this case as the subject will only be wearing the device for a short time, so a higher prediction

error is allowed. However, researchers might be in a hurry to set up the experiment and be less precise when performing the measurements. It is therefore in their best interest to select measurements that are not too sensitive to measurement errors. Upon considering
475 Table 5, the designer decides to use *arc length* instead of *head length*. He then creates a 3D design by varying the two parameters within certain ranges and making sure the product offers the right amount of adjustability. Using Fig. 7, he knows this design will accommodate at least 75% of the population. An example of the final result is shown in Fig. 15. Customizability can be achieved by turning the knob on the back of the
480 head. Even though certain parts of the headset do not make contact with all user's heads, the electrodes remain at the proper positions, so measurement accuracy is not compromised. Furthermore, markings can be made on the knob to indicate the position to which it should be adjusted for different head sizes. The researcher can thus simply use a look-up-table or computer program to instantly find the proper adjustment for a
485 specific test subject. This eliminates the need to rely on trial-and-error and decreases the preparation time required for the experiment.

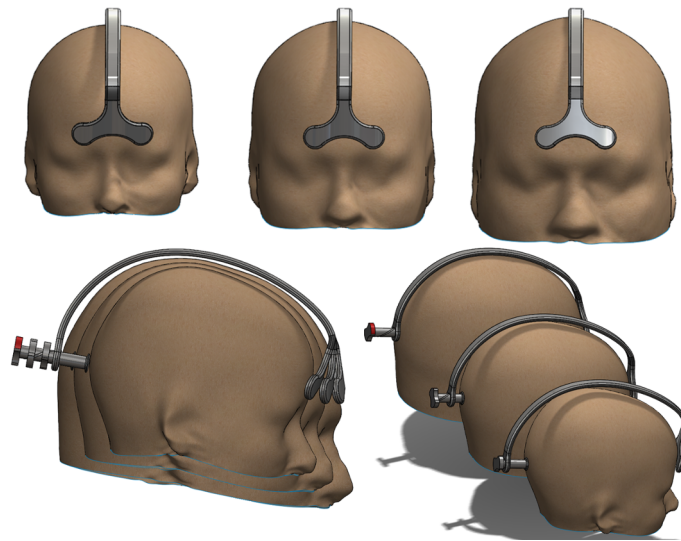


Figure 15: Example of an adjustable brain-computer interface headset created with the anthropometric shape model.

The above discussion gives a limited description of how the shape model can be used

to design one type of products. Other products that might benefit from anthropometric model design are sports and safety helmets, glasses, smart textiles and near-body sensors. 490 A complete description of the design process using anthropometric shape models is out of scope for this paper, but will be the theme of future work.

5. Conclusion

This work describes a method to create an anthropometric shape model from 100 MRI scans that can be used to accurately predict and analyze the shape of the human scalp 495 for a Western population. The shape model was parametrized by the anthropometric features *head length*, *face width*, *bitracion width*, *ear height*, *horizontal position of the ear*, *vertical position of the ear*, *projected ear height*, *circumference*, *arc length* and *arc width*. Several combinations of these anthropometric measurements offer good predictions, but the best one is obtained by combining all of them except for the *ear height* or *projected* 500 *ear height*: 1.60 ± 0.36 mm. The sample size was verified using a cross-validation analysis on the anthropometric model, which revealed that the average geometric error levels at a sample size of 90 individuals. The sensitivity of the model to errors in input measurements was analyzed and it was shown that the *arc length measurement* is the least sensitive to measurement errors, while the (*projected*) *ear height* is the most sensitive 505 one. Furthermore, the *ear height* seems to have no correlation with the overall shape of the head. It is not clear whether this is due to actual physical properties or due to the effect of the morphological operations that are applied to the input scans. It was shown that 3D scalp shapes generated with the proposed method look realistic and retain all information on the variability of the entire head. However, when the input measurements 510 lie in extreme ranges or when an incompatible combination of values is used, realism is no longer guaranteed. Further research is needed to find the correlations between all anthropometric measurements values and to determine the correct input boundaries.

Two use cases were demonstrated for the model. The first case is an application for anthropometric research, discussing the shape variability between the male and female 515 scalp. Using the anthropometric shape model, it was shown that the main difference between male and female head shapes is the overall size or volume of the head. Furthermore, when predicting a female scalps shape with a male shape model or vice versa, most

errors seem to be located in the region of the forehead. A literature review confirmed that the main differences between male and female skull are indeed the size of the head and the size of the eyebrow ridge. This demonstrates that the anthropometric shape model can be used to accurately find variations in shape between different populations. A second use case was the CAD design of an elementary brain-computer interface (BCI) headset for two types of use cases: assisted communication and BCI research. A CAD design of a BCI headset was created for both cases using the data presented in this paper. Because the CAD design was linked to the shape model, it could automatically be adapted to various head sizes while retaining the correct electrode positions. This implies that the anthropometric shape model can indeed be used to aid the design of BCI-headsets and other near-body products such as helmets or glasses.

The current results demonstrate the usability of a shape model parametrized by anthropometric measurements for ergonomic studies and design. In summary, to determine the optimal combination of anthropometric measurements for product design or analysis, the prediction accuracy, cumulative distribution and sensitivity should be taken into account. The importance of each of these factors depends on the intended application. By incorporating the anthropometric model into CAD software, digital designs can be directly driven and verified before prototyping. It is expected that the implementation of the proposed methodology will save time and significantly improve the design process.

6. Acknowledgments

Data collection and sharing for this project was provided by the International Consortium for Brain Mapping (ICBM; Principal Investigator: John Mazziotta, MD, PhD). ICBM funding was provided by the National Institute of Biomedical Imaging and Bio-Engineering. ICBM data are disseminated by the Laboratory of Neuro Imaging at the University of California, Los Angeles.

This work was partially supported by Interuniversity Attraction Poles Programme - Belgian Science Policy (IUAP), Grant number: IUAP P7/11, Institute for Technology (iMinds), a research institute founded by the Flemish Government, URL: <http://www.iminds.be/en>.

References

- [1] C. C. Wang, Parameterization and parametric design of mannequins, *Computer-Aided Design* 37 (1) (2005) 83–98.
- 550 [2] N. Magnenat-Thalmann, H. Seo, F. Cordier, Automatic modeling of virtual humans and body clothing, *J. Comput. Sci. Technol.* 19 (5) (2004) 575–584.
- [3] B. Allen, B. Curless, Z. Popovi, The space of human body shapes: reconstruction and parameterization from range scans, in: *ACM Transactions on Graphics (TOG)*, Vol. 22, 2003, p. 587594.
- [4] C.-H. Chu, Y.-T. Tsai, C. C. Wang, T.-H. Kwok, Exemplar-based statistical model for semantic
555 parametric design of human body, *Computers in Industry* 61 (6) (2010) 541–549.
- [5] S.-Y. Baek, K. Lee, Parametric human body shape modeling framework for human-centered product design, *Computer-Aided Design* 44 (1) (2012) 56–67.
- [6] S. Wuhrer, C. Shu, Estimating 3D human shapes from measurements, *Machine Vision and Applications* 24 (6) (2012) 1133–1147.
- 560 [7] V. Blanz, T. Vetter, A morphable model for the synthesis of 3D faces, in: *Proceedings of the 26th annual conference on Computer graphics and interactive techniques*, 1999, p. 187194.
- [8] P. Xi, C. Shu, Consistent parameterization and statistical analysis of human head scans, *The Visual Computer* 25 (9) (2009) 863–871.
- [9] P. Meunier, D. Tack, A. Ricci, L. Bossi, H. Angel, Helmet accommodation analysis using 3D laser
565 scanning, *Applied Ergonomics* 31 (4) (2000) 361369.
- [10] J. Niu, Z. Li, G. Salvendy, Multi-resolution description of three-dimensional anthropometric data for design simplification, *Applied Ergonomics* 40 (4) (2009) 807–810.
- [11] P. Meunier, C. Shu, P. Xi, Revealing the internal structure of human variability for design purposes, in: *Proceedings of the 17th World Congress on Ergonomics 2009*, 2009.
- 570 [12] Z. Zhuang, C. Shu, P. Xi, M. Bergman, M. Joseph, Head-and-face shape variations of U.S. civilian workers, *Applied Ergonomics* 44 (5) (2013) 775–784.
- [13] Y.-L. Lin, M.-J. J. Wang, Constructing 3D human model from front and side images, *Expert Systems with Applications* 39 (2012) 5012–5018.
- [14] B. Z. Allison, S. Dunne, R. Leeb, J. Del R. Milln, A. Nijholt, *Towards Practical Brain-Computer
575 Interfaces, Bridging the Gap from Research to Real-World Applications*, Springer, Heidelberg, 2012.
- [15] L. Capetillo-Cunliffe, *Loni: Laboratory of neuro imaging* (2007).
- [16] Z. Mai, R. Hanel, J. Batenburg, M. Verhoye, P. Scheunders, J. Sijbers, Bias field reduction by localized lloyd-max quantization, *Magnetic Resonance Imaging* 29 (2011) 536–545.
- [17] M. B. Dillencourt, H. Samet, M. Tamminen, A general approach to connected-component representations labeling for arbitrary image representations, *Journal of the Association for Computing
580 Machinery* 39 (2) (1992) 253–280.
- [18] M. Lepage, J. C. Gore, Contrast mechanisms in magnetic resonance imaging, *Journal of Physics: Conference Series* 3 (2004) 78–86.
- 585 [19] A. Simmons, P. S. Tofts, G. J. Barker, S. R. Arridge, Sources of intensity nonuniformity in spin echo images at 1.5 t, *Magnetic Resonance in Medicine* 32 (1) (1994) 121–128.

- [20] R. Kimmel, J. A. Sethian, Computing geodesic paths on manifolds, *Proceedings of the National Academy of Sciences* 95 (15) (1998) 8431–8435.
- [21] T. Huysmans, J. Sijbers, V. Brigitte, Automatic construction of correspondences for tubular surfaces, *IEEE Transactions on Pattern Analysis and Machine Intelligence* 32 (4) (2010) 636651.
- 590 [22] M. S. Floater, Parametrization and smooth approximation of surface triangulations, *Computer-Aided Design* 14 (1997) 231–250.
- [23] M. S. Floater, Mean value coordinates, *Computer Aided Geometric Design* 20 (1) (2003) 19–27.
- [24] R. Martin, K. Saller, *Lehrbuch der Anthropologie, in systematischer Darstellung*, Stuttgart, Fischer, Germany, 1957.
- 595 [25] Y. Cheng, W. K. Leow, T. C. Lim, Automatic identification of frankfurt plane and mid-sagittal plane of skull, in: *Applications of Computer Vision (WACV)*, 2012 IEEE Workshop on, IEEE, 2012, pp. 233–238.
- [26] M. Kouchi, M. Mochimaru, K. Tsuzuki, T. Yokoi, Interobserver errors in anthropometry, *Journal of Human Ergol.* 28 (1999) 15–24.
- 600 [27] M. Kouchi, M. Mochimaru, Errors in landmarking and the evaluation of the accuracy of traditional and 3d anthropometry, *Applied Ergonomics* 42 (3) (2011) 518–527.
- [28] A. Yu, K. Yick, S. Ng, J. Yip, 2d and 3d anatomical analyses of hand dimensions for custom-made gloves, *Applied Ergonomics* 44 (3) (2013) 381–392.
- [29] D. Formica, S. Silvestri, Biological effects of exposure to magnetic resonance imaging an overview, *BioMedical Engineering OnLine*.
- 605 [30] R. Ball, C. Shu, P. Xi, M. Rioux, Y. Luximon, J. Molenbroek, A comparison between chinese and caucasian head shapes, *Applied Ergonomics* 41 (6) (2010) 832–839.
- [31] G. Golub, V. L. C.F., *Matrix Computations*, 3rd ed., Johns Hopkins, Baltimore, 1996.
- [32] Z. Zhuang, D. Landsittel, S. Benson, R. Roberge, R. Shaffer, Facial anthropometric differences among gender, ethnicity, and age groups, *Annals of Occupational Hygiene* 54 (4) (2010) 391–402.
- 610 [33] M. K. Lee, O. Sakai, J. H. Spiegel, CT measurement of the frontal sinus gender differences and implications for frontal cranioplasty, *Journal of Cranio-Maxillofacial Surgery* 38 (7) (2010) 494–500.
- [34] E. Anibor, D. E. Eboh, M. O. Etetafia, A study of craniofacial parameters and total body height, *Pelagia Research Library, Advances in Applied Science Research* 2 (2011) 400–405.
- 615 [35] P. Brunner, I. Bianchi, C. Guger, F. Cincotti, G. Schalk, Current trends in hardware and software for brain-computer interfaces (BCIs), *Journal of Neural Engineering* 8 (2011) 7pp.
- [36] D. S. S. Corp, 3d CAD design software SolidWorks (2014).
- [37] N. Christis, *Anthropometrics 2.0*, Ph.D. thesis, Universiteit Antwerpen (2013).
- 620 [38] R. Oostenveld, P. Praamstra, The five percent electrode system for high-resolution EEG and ERP measurements, *Clinical neurophysiology* 112 (4) (2001) 713719.